Electronic Supplementary Material (ESI) for Journal of Materials Chemistry A.

Supporting information

Simulation Guided Molecular Design of Hydrofluoroether Solvent for High Energy Batteries

Zhou Yu[1,2+], Zhangxing Shi[1,3+], Sambasiva R. Bheemireddy[1,3], Ethan Kamphaus[1,2], Xingyi Lyu[4], Mohammad Afsar Uddin[1,5], Zhiguang Li[1,3,7], Zhenzhen Yang[1,3], Tao Li[1,4,6], Jeffrey S. Moore[1,5,8,9], Lu Zhang[1,3*], Lei Cheng[1,2*]

[1]Joint Center for Energy Storage Research, Argonne National Laboratory, Lemont, IL 60439, USA.
[2]Materials Science Division, Argonne National Laboratory, Lemont, IL 60439, USA
[3]Chemical Sciences and Engineering Division, Argonne National Laboratory, Lemont, IL 60439, USA
[4]Department of Chemistry and Biochemistry, Northern Illinois University, DeKalb, IL 60439, USA
[5]Department of Chemistry, University of Illinois at Urbana–Champaign, Urbana, IL 61801, USA
[6]X-ray Science Division, Argonne National Laboratory, Lemont, IL 60439, USA
[7]Indiana University-Purdue University Indianapolis, 723 West Michigan Street, Indianapolis, IN, 46202, USA
[8]Beckman Institute for Advanced Science and Technology, University of Illinois at Urbana–Champaign, Urbana, IL 61801, USA
[9]Department of Materials Science and Engineering, University of Illinois at Urbana–Champaign, Urbana, IL 61801, USA

[+]Zhou Yu and Zhangxing Shi contributed equally to this work.
* Corresponding Authors: Lu Zhang zhanglu77@gmail.com and Lei Cheng chengl@ornl

1. Theoretical Calculations

Table S1. Classical MD system setups

Name	Solvent No.	Ion No.	Box (nm)	C (M)
F2O2	500	100	5.475	1.012
F2O3	500	120	5.838	1.001
F3O2	500	120	5.748	1.049
F3O3	500	140	6.087	1.031
DME	500	60	4.659	0.985

Classical MD Simulation: The classical MD simulation system was composed of ~1 M lithium bis(trifluoromethanesulfonyl)imide (LiTFSI) and different solvents, including four newly synthesized fluorinated ethers (e.g., F2O2, F2O3, F3O2, F3O3) and dimethoxyethane (DME) shown in Table S1. The molecular geometries of these fluorinated ethers were generated from scratch and optimized with the universal force field[1] using the Avogadro program.[2] The initial configurations in classical MD simulations were packed using the Packmol code.[3] The simulation box is periodic in all three directions. The force fields of the system were built based on the OPLS-aa force field.[4] Specifically, the force fields of TFSI ion were extracted from the prior work,[5] and the force fields of the solvents were generated using the LigParGen code.[6-7]

The classical MD simulations were performed using the GROMACS code[8] with a 2 fs time step. First, a 50 ns equilibrium simulation was performed under the NPT ensemble for each system. The system energy, box size, and the solvation environment around Li ions are stable during the last 10 ns of the simulation. Then, a 250 ns production run was performed under the NVT ensemble. The Parrinello-Rahman barostat was used to maintain the system pressure at 1 atm with a time constant of 10 ps.[9] The V-rescale thermostat was used to stabilize the system temperature at 350 K with a time constant of 1 ps.[10] The electrostatic interactions were computed using the particle mesh Ewald (PME) method.[11] The real space cutoff and fast Fourier transform spacing were set to 1.2 and 0.12 nm, respectively. The non-electrostatic interactions were computed by direct summation with a cutoff length of 1.2 nm. The last 200 ns trajectory in the production run was used for analysis.

Table S2. AIMD system setups

Name	Position of salt	DME No.	FXO3 No.	LiTFSI No.	Box (Å^3)
DME_middle	middle	17	/	2	14.04 × 14.04 × 27.63
DME_interface	interface	17	/	2	14.04 × 14.04 × 27.63
F2O3_middle	middle	/	8	2	14.04 × 14.04 × 27.30
F2O3_interface	interface	/	8	2	14.04 × 14.04 × 27.30
F3O3	middle & interface	/	7	2	14.04 × 14.04 × 26.72

Ab Initio MD Simulation: *Ab initio* MD system is composed of a Li metal electrode and a slab of electrolyte. The most stable (1 0 0) surface has been used for the Li electrode.[12] Meanwhile, the Li electrode has seven layers, and the center three layers have been fixed during the simulation. The simulation box is periodic in all three directions. The space between electrodes is thicker than 16.50 Å. The concentration of LiTFSI in all simulations is ~1 M. The *ab initio* MD system setups are summarized in Table S2. The initial configurations for the *Ab initio* MD simulations with LiTFSI in the middle of the electrolyte or at the interface between electrode and electrolyte were packed using the Packmol code.[3] The system was firstly relaxed through classical MD simulation. The *ab initio* MD simulations were then carried out using the VASP code.[13-14] The projector augmented waves (PAW) method was used to compute the interatomic forces with the Perdew–Burke–Ernzerhof (PBE) generalized gradient approximation for the exchange-correlation energy.[15-16] The plane waves energy cutoff was set as 400 eV. The Brillouin zone was sampled at the Γ-point.[17] The convergence criteria for the electronic self-consistency and ionic relaxation loop were set to 10^{-5} and 10^{-4} eV, respectively. The time step is 1 fs and the temperature is 350 K. A 10 ps trajectory was produced for each system under the NVT ensemble with Nose-Hoover thermostat for the analysis of the interfacial reaction. Meanwhile, we performed Bader charge analysis on each system in order to elucidate the electronic distribution.[18-21] Specifically, 100 frames were extracted from a 10 ps trajectory of each simulation with a time interval of 100 fs, and single point calculations were performed for each frame.

Quantum Chemical Cluster Calculation: The molecular geometries were optimized at the DFT level with the B3LYP/6-31+G(d,p) and M052X/6-31+G(d,p) method using the Gaussian program.[22] The energies of the highest occupied molecular orbital (HOMO) and lowest unoccupied molecular orbital (LUMO) were obtained from the optimized geometry.

Single-linkage clustering algorithm: For the ionic aggregate analysis, we start from a Li ion and search the O atom in TFSI ions within the cutoff distance, which corresponds to the location of the first valley in the RDF from Li ion to O atom in TFSI ion shown in Figure S2. If no O atoms were found, we choose another Li ion and carry out the previous step. Otherwise, we consider all four O atoms in the newly found TFSI ion as the center atoms and search for the other neighboring Li ions within the cutoff distance. The process is repeated until no new Li ion is found.

For the aggregates composed of F/O in solvent molecules, we start from a F/O atom in a solvent molecule and search for other F/O atoms in solvent molecules within the cutoff distance, which corresponds to the location of the first valley in the RDF between F/O in solvent molecules shown in Figure S6. Then we regard the newly found F/O atoms as the center atoms and repeat the previous step. If no new F/O atoms were found, the search process was conducted from another F/O atom until there is no new F/O atom in solvent molecules.

Li-TFSI association correlation function: To characterize the lifetime of Li-TFSI ion pair in different electrolytes (see Figure S9), we calculated the Li-TFSI association correlation function following $ACF(t) = \langle c(0)c(t) \rangle$, where $c(t)$ is an indicator of the Li-TFSI association. $c(t)$ is 1.0 if a TFSI ion coordinating with a Li ion at time 0 is continuously stay in the first solvation shell of this Li ion by time t. The correlated function can be fitted to the stretched exponential function following $ACF(t) = a_0 exp(- (t/a_1)^{a_2})$. Then, the lifetime of the Li-TFSI ion pair is calculated according to the fitting parameters a_0, a_1, and a_2 following the gamma function $\tau_{ij} = a_0 a_1 \Gamma(1 + 1/a_2)$.

Diffusivity and conductivity calculation: The self-diffusivity of ions and solvents and the ionic conductivity of electrolytes are calculated according to the following equations: $D_A = \frac{1}{6t} \lim_{t \to \infty} \langle |R_i(t) - R_i(0)|^2 \rangle_{i \in A}$ and $\sigma = \lim_{t \to \infty} \frac{e^2}{6tVk_BT} \sum_{ij}^{N} Z_i Z_j \langle [R_i(t) - R_i(0)][R_j(t) - R_j(0)] \rangle$. Where D_A is the self-diffusivity of A, $R_i(t)$ is coordinates of *i* at time t, σ is the ionic conductivity, *V* is the volume of the system, *T* is temperature, and Z_i is the charge on *i*.

2. Materials and Syntheses

Fluorinated ethers were obtained by using the following general synthesis procedure. To a suspension of NaH (1 eq) in DMF was added fluorinated alcohol (1 eq) dropwise under a nitrogen atmosphere at 0 °C. This mixture was stirred at 0 °C for 20 minutes and at room temperature for 10 minutes. Then, Bromo ether (0.5 eq) starting material was added to the reaction mixture dropwise at room temperature, and the reaction was stirred overnight before water was added. The final products were obtained by diethyl ether extraction.

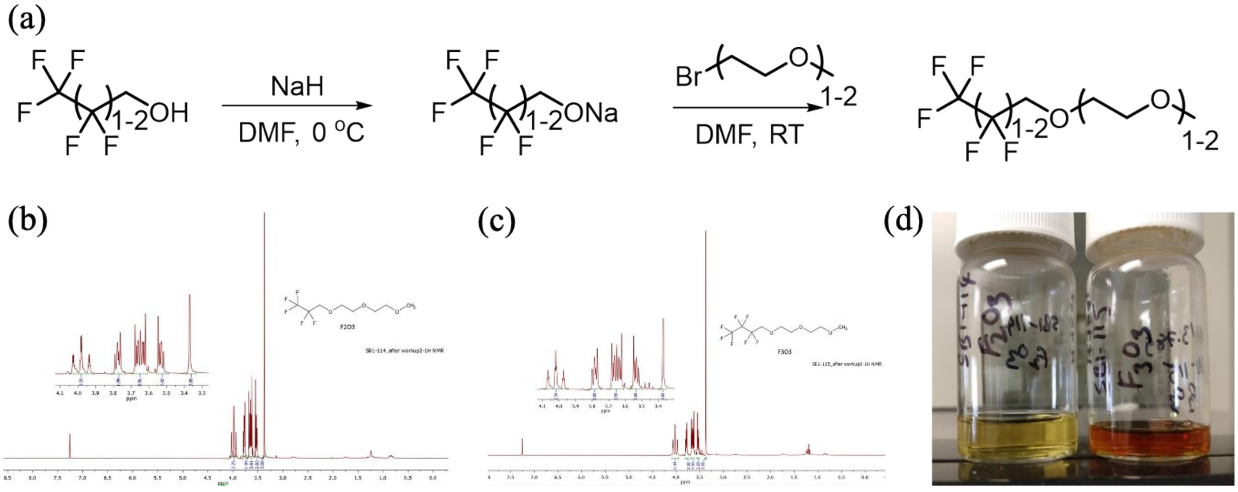

Figure S1. (a) Representative synthetic scheme.

3. Material Characterizations

Raman spectroscopy. Raman experiments were conducted with a Renishaw confocal micro-Raman system at the Center for Nanoscale Materials of Argonne National Laboratory. The samples were first sealed in quartz capillaries and measured within the capillaries. The quartz capillary has no Raman bands, so background correction is not required. Raman excitation was applied with laser wavelengths of 532 nm. Raman spectra were recorded using a 50× focusing/collection optic with a numerical aperture of 0.5 (Leica).

X-ray photoelectron spectroscopy. After rinsing the electrodes, the samples were transferred, without air exposure, to the XPS chamber (Physical Electronics), which is attached to an Ar-atmosphere glovebox. The high resolution spectra were obtained using a 100 μm beam (25 W) with Al Kα radiation (hυ = 1486.6 eV), Ar^{+-} ion and electron beam sample neutralization, fixed analyzer transmission mode, and pass energy of 23.25 eV. For data analysis of all spectra, the Shirley background was subtracted, and the resulting spectrum was fitted to multiple Gaussian peaks using Multipak software provided by Physical Electronics.

4. Electrochemical Measurements

The cycling performance of lithium metal cells was evaluated using 2032-type stainless steel coin cells. The cells were configured with a lithium metal electrode, a microporous polypropylene separator (Celgard 2325), an NMC 622 cathode, and 25 μL of electrolyte containing 10 wt% FEC. The cells were first subjected to three formation cycles at a C/10 rate followed by 100 cycles at a C/3 rate with the cell voltage maintained between 3.0 to 4.2 V during this cycling. The current rate was derived from the actual capacity during the formation cycle.

The ionic conductivity of electrolytes was measured by conducting electrochemical impedance spectroscopy (EIS, Figure S14) on an assembled testing cell. A 2032-coin cell was assembled consisting of a Teflon ring sandwiched between two stainless steel spacers. Electrolyte samples were filled in the space between the spacers. The EIS was con in the frequency range from 1 MHz to 0.1 Hz. Ionic conductivity can be calculated using the Z’ intercept at a high frequency range obtained from the Nyquist plot of the EIS spectrum. F2O3 and F3O3 electrolytes show ionic conductivity values of 1.81 and 0.76 mS/cm, respectively.

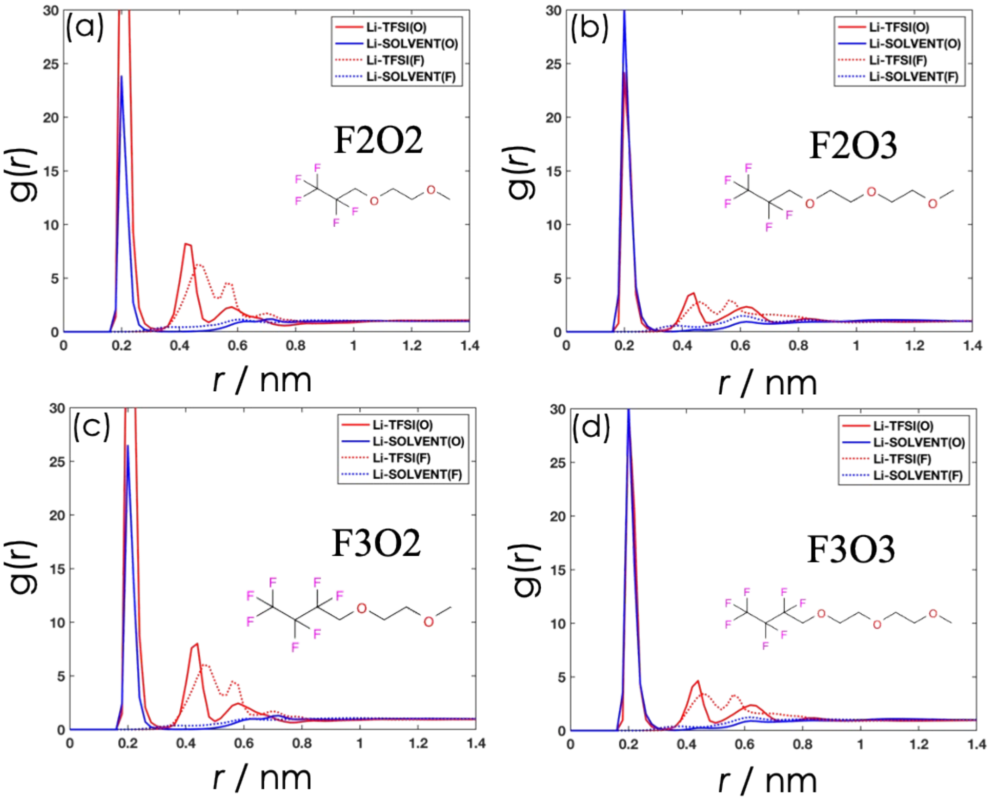

Figure S2. Radial distribution function (RDF) from Li ion to O and F in TFSI ion and fluorinated ethers.

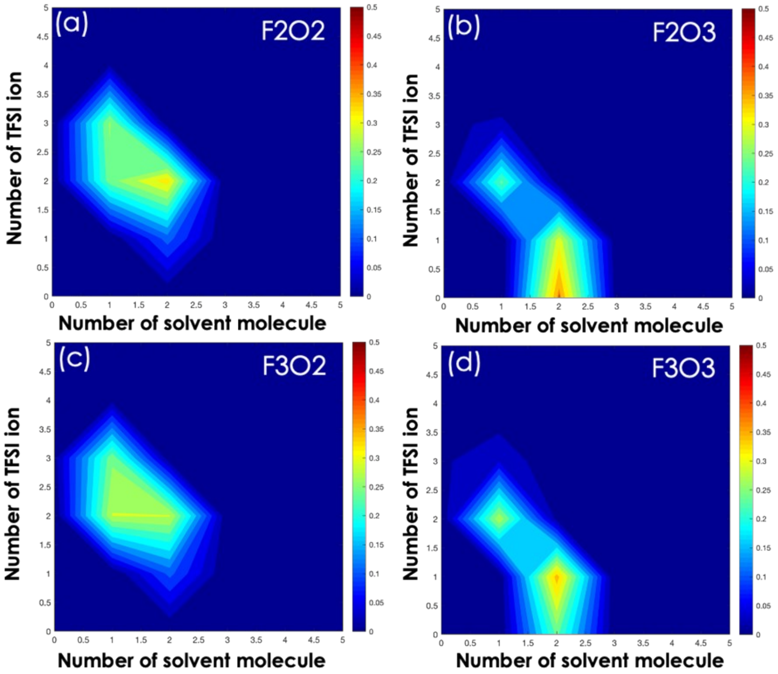

Figure S3. Time-averaged appearance frequency of the coordination number (CN) of TFSI ions and solvent molecules in the first solvation shell of Li ion in different electrolytes. The color bar represents the occurrence frequency.

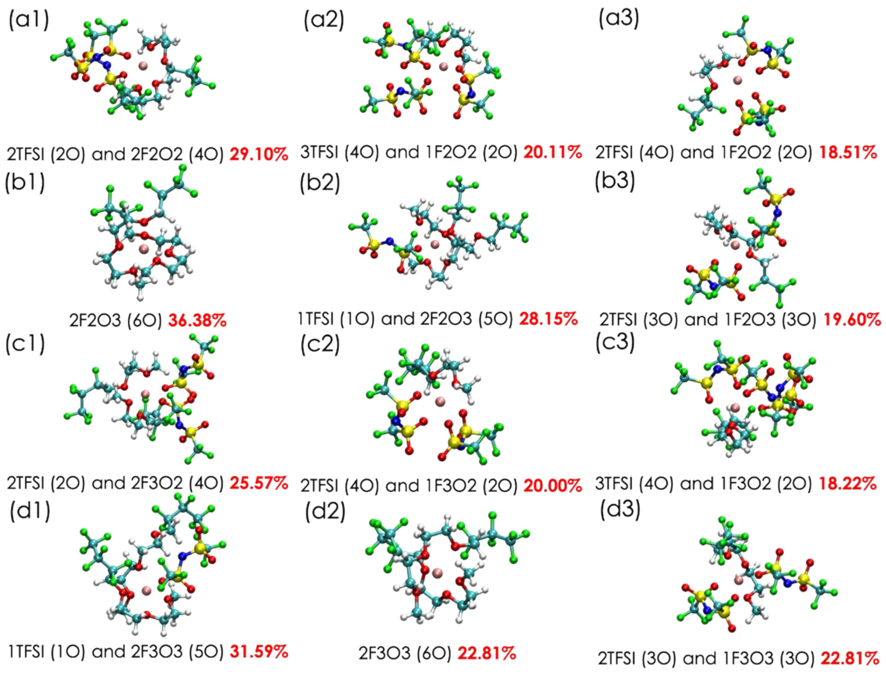

(a1) 2TFSI (2O) and 2F2O2 (4O) **29.10%**
(a2) 3TFSI (4O) and 1F2O2 (2O) **20.11%**
(a3) 2TFSI (4O) and 1F2O2 (2O) **18.51%**
(b1) 2F2O3 (6O) **36.38%**
(b2) 1TFSI (1O) and 2F2O3 (5O) **28.15%**
(b3) 2TFSI (3O) and 1F2O3 (3O) **19.60%**
(c1) 2TFSI (2O) and 2F3O2 (4O) **25.57%**
(c2) 2TFSI (4O) and 1F3O2 (2O) **20.00%**
(c3) 3TFSI (4O) and 1F3O2 (2O) **18.22%**
(d1) 1TFSI (1O) and 2F3O3 (5O) **31.59%**
(d2) 2F3O3 (6O) **22.81%**
(d3) 2TFSI (3O) and 1F3O3 (3O) **22.81%**

Figure S4. Representative solvation structures around Lis in F2O2, F2O3, F3O2, and F3O3 systems, respectively. The fraction of each solvation structures is marked in red. Pink, blue, yellow, red, cyan, and green balls denote Li, N, S, O, C, and F, respectively.

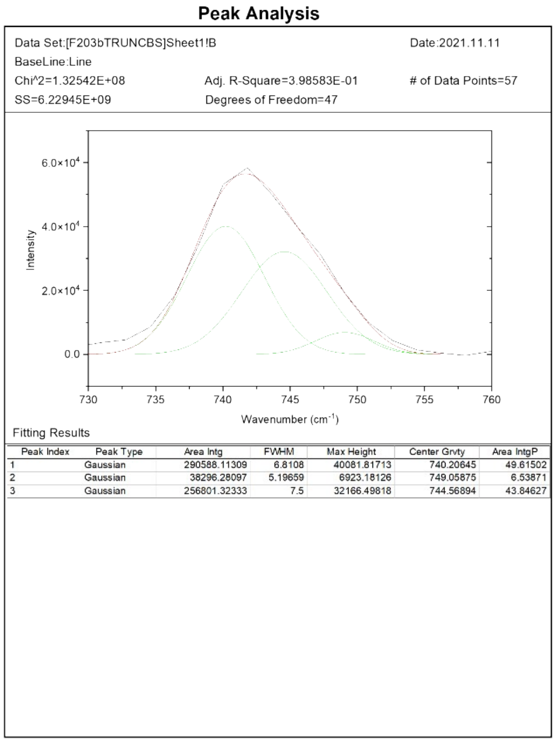

Peak Analysis

Data Set:[F203bTRUNCBS]Sheet1!B Date:2021.11.11
BaseLine:Line
Chi^2=1.32542E+08 Adj. R-Square=3.98583E-01 # of Data Points=57
SS=6.22945E+09 Degrees of Freedom=47

Fitting Results

Peak Index	Peak Type	Area Intg	FWHM	Max Height	Center Grvty	Area IntgP
1	Gaussian	290588.11309	6.8108	40081.81713	740.20645	49.61502
2	Gaussian	38296.28097	5.19659	6923.18126	749.05875	6.53871
3	Gaussian	256801.32333	7.5	32166.49818	744.56894	43.84627

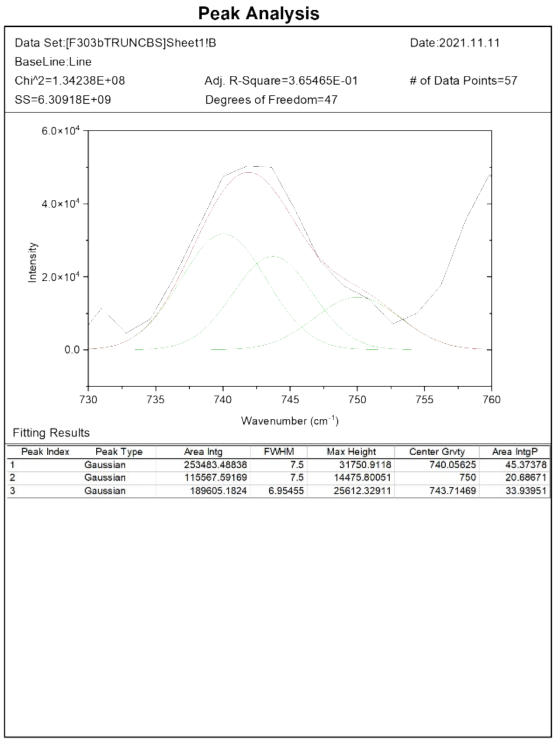

Peak Analysis

Data Set:[F303bTRUNCBS]Sheet1!B Date:2021.11.11
BaseLine:Line
Chi^2=1.34238E+08 Adj. R-Square=3.65465E-01 # of Data Points=57
SS=6.30918E+09 Degrees of Freedom=47

Fitting Results

Peak Index	Peak Type	Area Intg	FWHM	Max Height	Center Grvty	Area IntgP
1	Gaussian	253483.48838	7.5	31750.9118	740.05625	45.37378
2	Gaussian	115567.59169	7.5	14475.80051	750	20.68671
3	Gaussian	189605.1824	6.95455	25612.32911	743.71469	33.93951

Figure S5. Raman Spectral deconvolution for 1 M LiTFSI in F2O3 and F3O3.

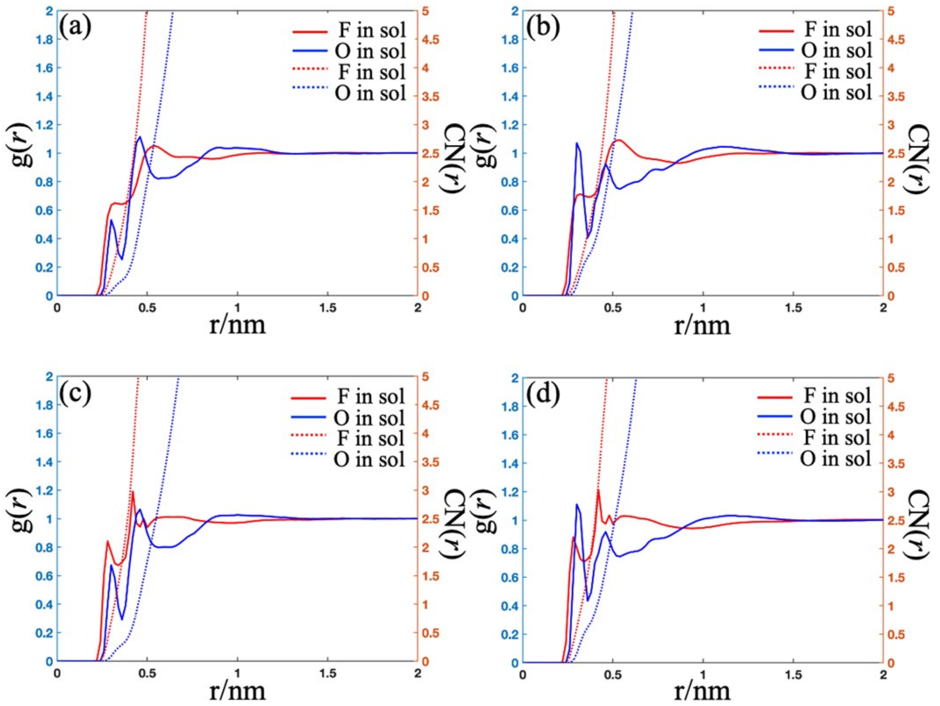

Figure S6. RDF and CN between F or O in the electrolytes with (a) F2O2, (b) F2O3, (c) F3O2, and (d) F3O3. The intramolecular F or O interaction is excluded.

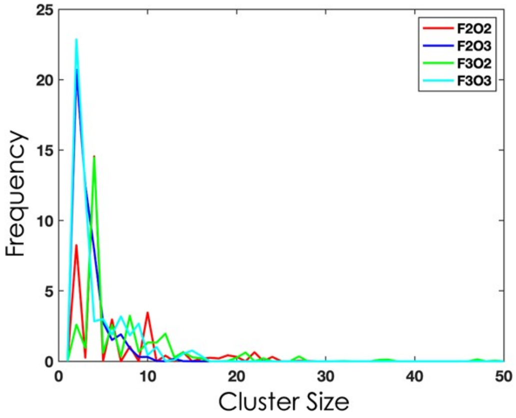

Figure S7 Time-averaged appearance frequency of ionic aggregates composition in different electrolytes. 500 frames were extracted from a 20 ns trajectory of each simulation with a time interval of 40 ps.

Table S3. Electrolytes nanostructure

	MaxF/TotF Cutoff=0.36 nm	AveO Cutoff=0.36 nm	AveO Cutoff=0.46 nm	AveIon	Free solvent
F2O2	95.77%	2.28	8.00	5.88	70.93%
F2O3	85.54%	3.58	34.06	1.69	59.66%
F3O2	99.37%	2.30	5.77	7.18	66.79%
F3O3	97.90%	3.60	21.19	2.28	55.74%

*MaxF/TotF represents the fraction of F atoms in solvent molecules forming the maximal cluster. AveO and AveIon represents the average number of O atoms in solvent molecules and ions (e.g., Li^+ and $TFSI^-$ ion) in each cluster, respectively.

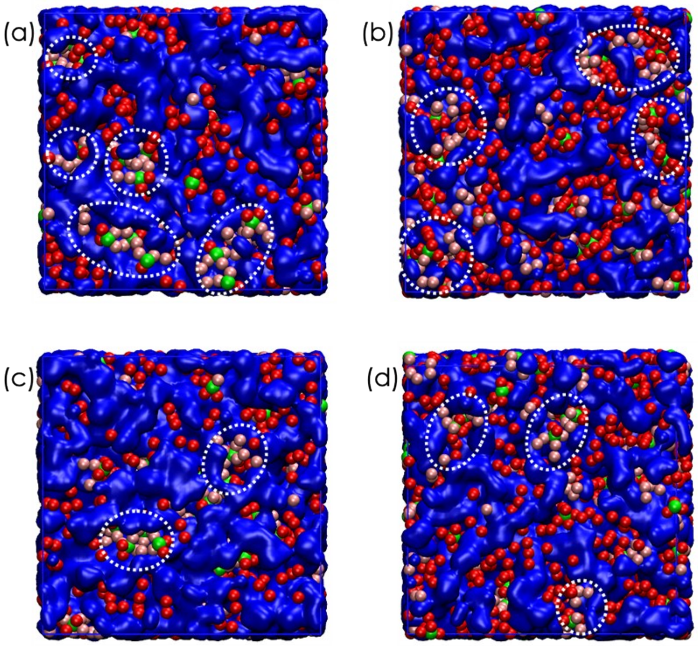

Figure S8. Snapshot of solution structure in 1 M LiTFSI (a) F2O2 (b) F2O3 (c) F3O2 (d) F3O3 electrolytes. Blue region represents F in solvent molecules and TFSI ions. Green, red, and pink balls denote Li, O in solvent and TFSI ion, respectively. White dotted cycles indicate some localized high concentration regions.

Table S4. Transport properties in different electrolytes. L represents the characteristic length.

Name	D-Li (10^{-11} m^2/s)	D-TFSI (10^{-11} m^2/s)	D-Solvent (10^{-11} m^2/s)	Conductivity (mS/cm)	Lifetime (ns)	L (Å)
F2O2	4.77 ± 0.07	4.53 ± 0.05	38.94 ± 0.10	0.1950 ± 0.0114	28.69	28.65
F2O3	3.07 ± 0.02	3.21 ± 0.01	9.41 ± 0.12	1.1177 ± 0.0023	3.76	8.33
F3O2	3.06 ± 0.06	2.94 ± 0.04	20.54 ± 0.07	0.1392 ± 0.0080	29.47	23.26
F3O3	0.94 ± 0.01	1.16 ± 0.01	4.31 ± 0.02	0.3873 ± 0.0010	7.79	6.63

Vehicular and structural motions are two representative transport mechanisms of ions in electrolytes. Vehicular motion represents cation can diffuse with its solvation shell as one species. Structural motion means the cation can diffuse through the continuous exchange of its solvation shell composed of anion and solvent molecules. The transport mechanism of a Li ion as the reference of the TFSI ion in its solvation shell is determined by the characteristic length following

$L_{Li-TFSI}=\sqrt{6D_{Li}\tau_{Li-TFSI}}$, where D_{Li} is the self-diffusivity of Li ion and $\tau_{Li-TFSI}$ is the lifetime of the Li-TFSI ion pair. Essentially, $L_{Li-TFSI}$ describe how long the Li-TFSI ion pair can move before the dissociation of the ion pair occur. Therefore, smaller $L_{Li-TFSI}$ means the diffusion of Li ion tends to apply the structure motion through the continuous exchange of its associated TFSI ion. From Table S4, we can see the increase of O-segments length makes the diffusion of Li ion shift to the structural motion. This is because Li ion is coordinated by more O from solvent and less O from TFSI with the increase of solvent's O-segment length. The binding between Li and TFSI ion weakens, which helps the dissociation of the ion pair.

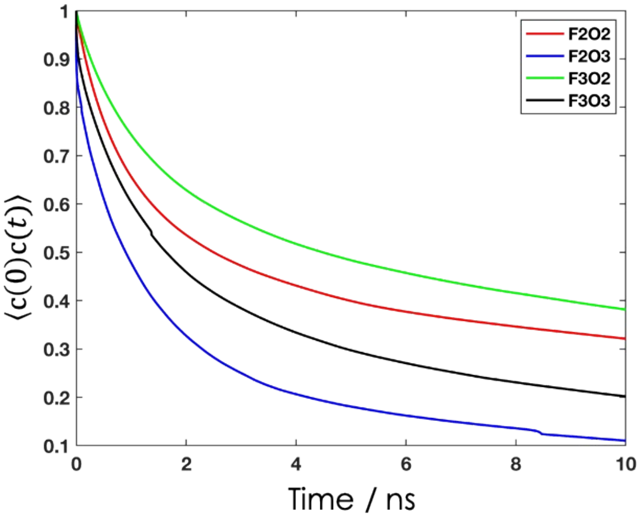

Figure S9. Li-TFSI association correlation function in electrolytes with different fluorinated ethers.

Table S5. LUMO and HOMO energy of the fluorinated ethers and DME

	B3LYP/6-31+G(d,p)		M052X/6-31+G(d,p)	
	LUMO (eV)	HOMO (eV)	LUMO (eV)	HOMO (eV)
F2O2	-0.275	-7.488	-0.346	-9.414
F2O3	-0.266	-7.244	-0.337	-9.167
F3O2	-0.275	-7.493	-0.346	-9.421
F3O3	-0.270	-7.338	-0.341	-9.292
DME	0.350	-7.136	1.551	-9.059

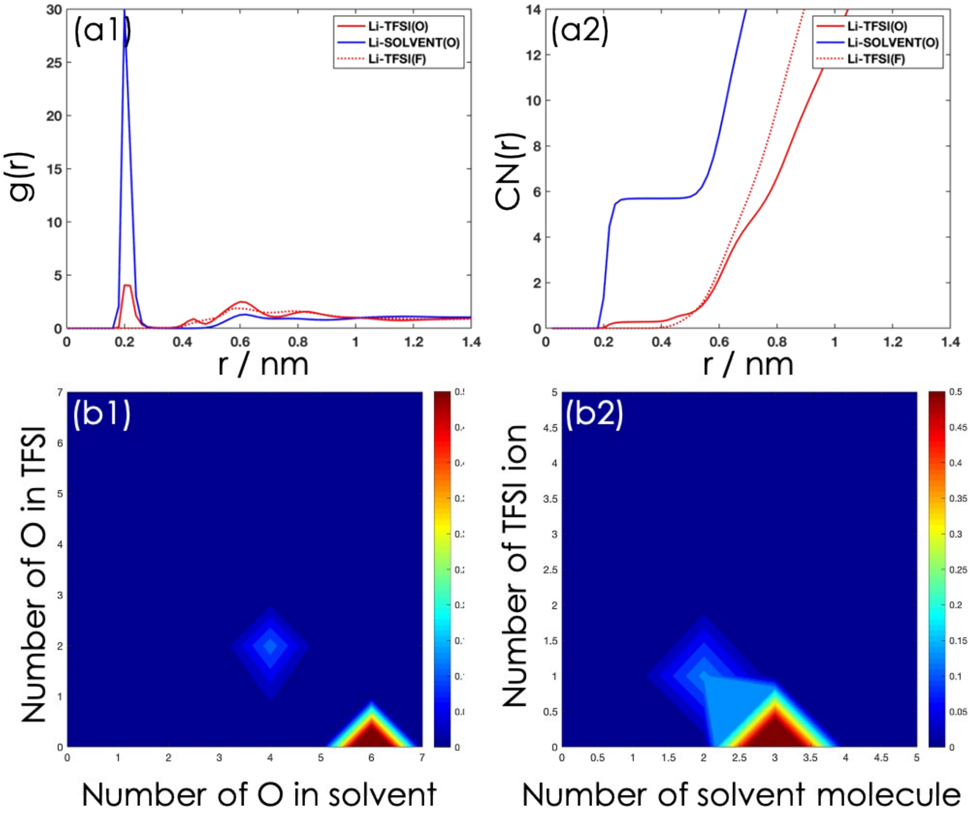

Figure S10. (a1) Radial distribution function from Li ion to O in TFSI and DME and F in TFSI. (a2) Coordination number of O in TFSI and DME and F in TFSI around Li ion. Time-averaged appearance frequency of the CN of (b1) O in TFSI ions and solvent molecules or (b2) TFSI ions and solvent molecules around Li ion in 1 M LiTFSI DME electrolyte. The fraction of free/SSIP, CIP, and AGG in the DME electrolyte is 84.18%, 12.45%, and 3.37%, respectively.

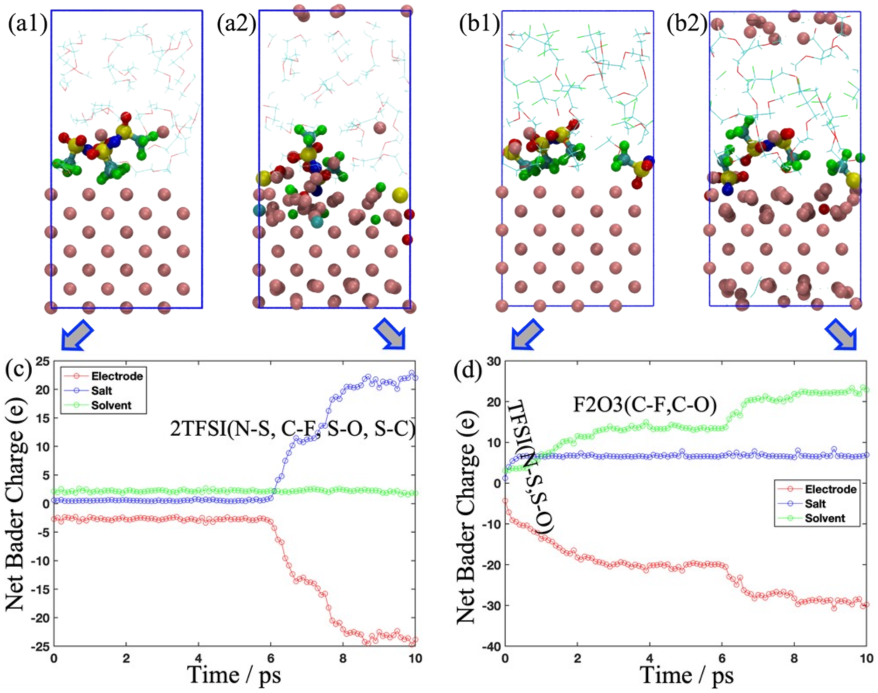

Figure S11. The initial and final snapshots extracted from AIMD simulations with (a) DME as solvent or (b) F2O3 as solvent. LiTFSI locates at the interface between electrode and electrolyte in the initial configuration. Pink, blue, yellow, red, cyan, and green balls denote Li, N, S, O, C, and F, respectively. The solvent molecules are depicted as wireframe. (c-d) Net Bader charges of system components.

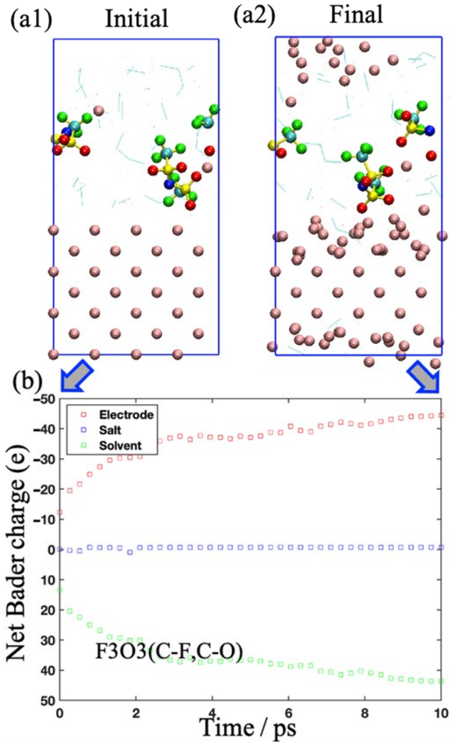

Figure S12. The initial and final snapshots extracted from AIMD simulations with F3O3 as solvent. Pink, blue, yellow, red, cyan, and green balls denote Li, N, S, O, C, and F, respectively. The solvent molecules are depicted as wireframe. (b) Net Bader charges of system components.

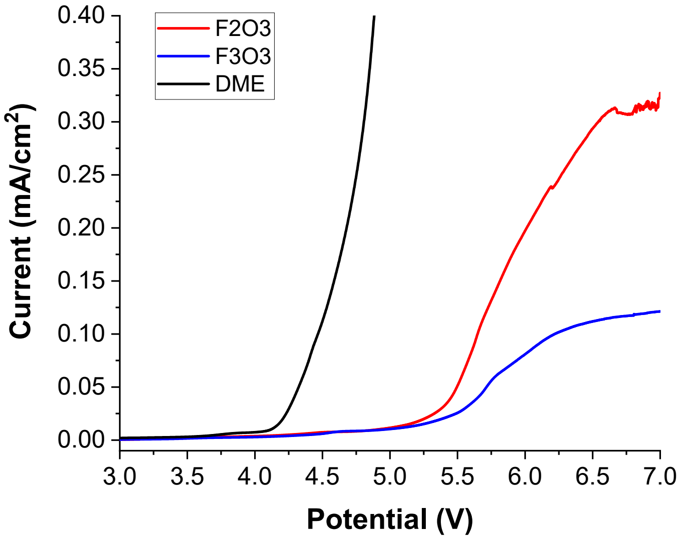

Figure S13. Linear sweep voltammetry (LSV) tests in 2032-type coin cell consists of a Li metal anode, a Celgard 2325 separator, a Al foil as counter electrode and 1 M LiTFSI in F2O3, F3O3 or DME electrolyte. The cells were subjected to a constant voltage sweep from 2.7 V to 7.0 V at a rate of 10 mV/s. F2O3 electrolyte shows excellent oxidative stability with no obvious decomposition until 5.5 V.

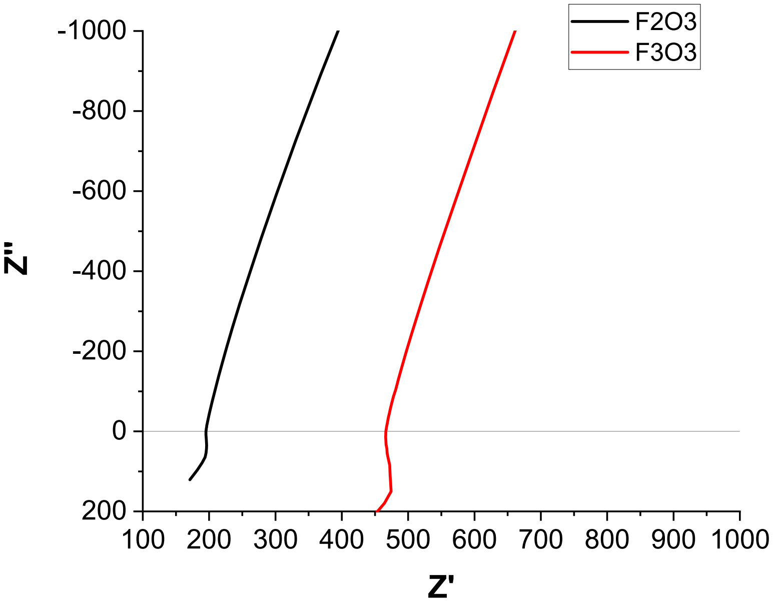

Figure S14. The ionic conductivity of the F2O3 and F3O3 electrolyte was measured using electrochemical impedance spectroscopy (EIS). The 2032-type coin cell used for the test consist of a Teflon ring that filled with F2O3 electrolyte that is sandwiched between two stainless steel current collectors. The electrochemical impedance of the cell was tested in the frequency range from 1 MHz to 0.1 Hz. Ionic conductivity can be calculated using the Z' intercept at a high frequency range obtained from the Nyquist plot of the EIS spectrum. F2O3 electrolyte shows high ionic conductivity of 1.81 mS/cm.

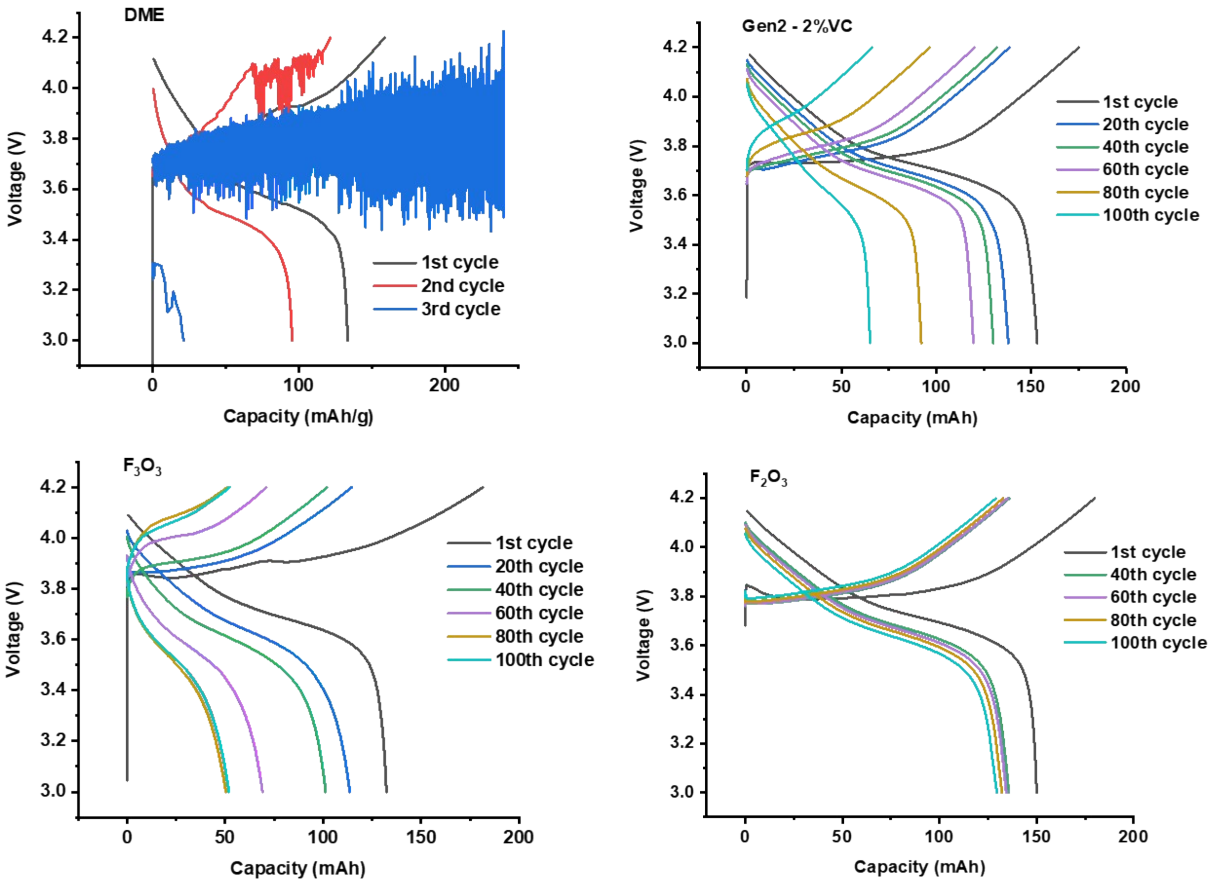

Figure S15. Voltage-capacity profiles for cells containing 1 M LiTFSI DME/F2O3/F3O3 electrolytes and 1 M LiPF6 in EC/EMC (3/7) plus 2% vinylene carbonate electrolyte.

Reference:

[1] Rappé, A. K.; Casewit, C. J.; Colwell, K.; Goddard III, W. A.; Skiff, W. M., Uff, a Full Periodic Table Force Field for Molecular Mechanics and Molecular Dynamics Simulations. *Journal of the American chemical society* **1992,** *114*, 10024-10035.

[2] Hanwell, M. D.; Curtis, D. E.; Lonie, D. C.; Vandermeersch, T.; Zurek, E.; Hutchison, G. R., Avogadro: An Advanced Semantic Chemical Editor, Visualization, and Analysis Platform. *Journal of cheminformatics* **2012,** *4*, 1-17.

[3] Martínez, L.; Andrade, R.; Birgin, E. G.; Martínez, J. M., Packmol: A Package for Building Initial Configurations for Molecular Dynamics Simulations. *Journal of computational chemistry* **2009,** *30*, 2157-2164.

[4] Jorgensen, W. L.; Maxwell, D. S.; Tirado-Rives, J., Development and Testing of the Opls All-Atom Force Field on Conformational Energetics and Properties of Organic Liquids. *Journal of the American Chemical Society* **1996,** *118*, 11225-11236.

[5] Doherty, B.; Zhong, X.; Gathiaka, S.; Li, B.; Acevedo, O., Revisiting Opls Force Field Parameters for Ionic Liquid Simulations. *Journal of chemical theory and computation* **2017,** *13*, 6131-6145.

[6] Dodda, L. S.; Vilseck, J. Z.; Tirado-Rives, J.; Jorgensen, W. L., 1.14* Cm1a-Lbcc: Localized Bond-Charge Corrected Cm1a Charges for Condensed-Phase Simulations. *The Journal of Physical Chemistry B* **2017,** *121*, 3864-3870.

[7] Dodda, L. S.; Cabeza de Vaca, I.; Tirado-Rives, J.; Jorgensen, W. L., Ligpargen Web Server: An Automatic Opls-Aa Parameter Generator for Organic Ligands. *Nucleic acids research* **2017,** *45*, W331-W336.

[8] Abraham, M. J.; Murtola, T.; Schulz, R.; Páll, S.; Smith, J. C.; Hess, B.; Lindahl, E., Gromacs: High Performance Molecular Simulations through Multi-Level Parallelism from Laptops to Supercomputers. *SoftwareX* **2015,** *1*, 19-25.

[9] Parrinello, M.; Rahman, A., Polymorphic Transitions in Single Crystals: A New Molecular Dynamics Method. *Journal of Applied physics* **1981,** *52*, 7182-7190.

[10] Bussi, G.; Donadio, D.; Parrinello, M., Canonical Sampling through Velocity Rescaling. *The Journal of chemical physics* **2007,** *126*, 014101.

[11] Darden, T.; York, D.; Pedersen, L., Particle Mesh Ewald: An N· Log (N) Method for Ewald Sums in Large Systems. *The Journal of chemical physics* **1993,** *98*, 10089-10092.

[12] Camacho-Forero, L. E.; Smith, T. W.; Bertolini, S.; Balbuena, P. B., Reactivity at the Lithium–Metal Anode Surface of Lithium–Sulfur Batteries. *The Journal of Physical Chemistry C* **2015,** *119*, 26828-26839.

[13] Kresse, G.; Hafner, J., Ab Initio Molecular-Dynamics Simulation of the Liquid-Metal–Amorphous-Semiconductor Transition in Germanium. *Physical Review B* **1994,** *49*, 14251.

[14] Kresse, G.; Furthmüller, J., Efficiency of Ab-Initio Total Energy Calculations for Metals and Semiconductors Using a Plane-Wave Basis Set. *Computational materials science* **1996,** *6*, 15-50.

[15] Kresse, G.; Joubert, D., From Ultrasoft Pseudopotentials to the Projector Augmented-Wave Method. *Physical review b* **1999,** *59*, 1758.

[16] Perdew, J. P.; Burke, K.; Ernzerhof, M., Generalized Gradient Approximation Made Simple. *Physical review letters* **1996,** *77*, 3865.

[17] Monkhorst, H. J.; Pack, J. D., Special Points for Brillouin-Zone Integrations. *Physical review B* **1976,** *13*, 5188.

[18] Henkelman, G.; Arnaldsson, A.; Jónsson, H., A Fast and Robust Algorithm for Bader Decomposition of Charge Density. *Computational Materials Science* **2006,** *36*, 354-360.

[19] Tang, W.; Sanville, E.; Henkelman, G., A Grid-Based Bader Analysis Algorithm without Lattice Bias. *Journal of Physics: Condensed Matter* **2009,** *21*, 084204.

[20] Yu, M.; Trinkle, D. R., Accurate and Efficient Algorithm for Bader Charge Integration. *The Journal of chemical physics* **2011,** *134*, 064111.

[21] Sanville, E.; Kenny, S. D.; Smith, R.; Henkelman, G., Improved Grid-Based Algorithm for Bader Charge Allocation. *Journal of computational chemistry* **2007,** *28*, 899-908.

[22] Frisch, M.; Trucks, G.; Schlegel, H.; Scuseria, G.; Robb, M.; Cheeseman, J.; Scalmani, G.; Barone, V.; Petersson, G.; Nakatsuji, H., Gaussian 16, Gaussian. *Inc., Wallingford CT* **2016,** *2016*.